Proceedings World Geothermal Congress 2023
Beijing, China, October 2023

Transport and clogging of colloidal particles: effects of concentration and geometry of the porous medium.

Esneu Anne-Sophie[1,2*], Marlière Claire[1], Nabzar Lahcen[1], Erriguible Arnaud[2], Glockner Stéphane[2], Marre Samuel[3] and Boujlel Younsi Jalila[1]

[1]IFP Energies Nouvelles, 1-4 Avenue du Bois Préau, 92852 Rueil-Malmaison, France

[2]CNRS, Univ. Bordeaux, Bordeaux INP, I2M, UMR 5295, 33600 Pessac, France

[3]CNRS, Univ. Bordeaux, Bordeaux INP, ICMCB, UMR 5026, 33600 Pessac, France

*anne-sophie.esneu@ifpen.fr

Keywords: colloids, clogging, porous media, micromodels, geothermal energy

ABSTRACT

Colloidal transport and deposition in porous media are complex processes that result from the interaction between hydrodynamics (velocity, pore geometry, …) and DLVO forces (particle-particle and particle-surface). They have a significant implication for engineering applications involving the reinjection of a fluid into a medium such as in geothermal energy. Investigation of the permeability stability is critical to ensure the sustainability of the activities. The aim of this work is to study clogging mechanisms in a rock-like porous medium using a microfluidic device. The pore-throat network distributions show that the micromodel geometry mimics real rock samples. The transport of a monodispersed suspension is studied at different concentrations. Image analysis, combined with a modeling of velocity fields, and pressure drop measurement are used to assess respectively preferential clogging sites and porous medium permeability reduction. Experiments show that retention sites are located around preferential flow paths where flow velocities are higher. When clogged, the pore thresholds are the deposition zones that lead to a reduction in permeability. However, pore bodies may also constitute deposit zones. It is interesting to highlight that as the concentration of the suspension increases, the kinetics of permeability reduction is delayed, and the clogging mechanisms as well as the type of deposit evolve. Finally, at very high concentrations, the effects of hydrodynamic stripping are more important. These observations emphasize the role of the porous medium geometry on colloidal transport and deposition and thus permeability reduction.

1. INTRODUCTION

Geothermal fluids are often loaded with mineral and organic particles in suspension, dissolved organic and mineral compounds, various additives, bacteria, heavy metals, etc. These compounds pose significant problems on the sustainability of production and the maintenance of injectivity in the short term and, in the long term, on the stability and continuity of the resource. As the migration and deposit of fines concern numerous industrial applications, the physics of colloidal particles in porous media has been widely studied.

Historically, studies undertaken to investigate flow behavior and the associated mechanisms, whether physical or chemical, are based on macroscopic measurements, mostly with corefloods: usually, a core sample from a geomaterial (rock) is submitted to a flow experiment performed under reservoir conditions. The pressure drop obtained along the medium enables the measurre of some important parameters such as permeability and the characterization of their evolution over time. However, since these media are opaque, we lack information on the mechanisms involved at the pore scale and direct characterization of flow and particle transport within the pore space is not possible with the tools previously mentioned. However, new sophisticated investigation methods allow access to the pore scale such as 3D and 4D X-ray (micro) computed tomography (CT, µCT), magnetic resonance imaging (MRI), nuclear magnetic resonance (NMR), microfluidics and others (Jahanbakhsh et al., 2020).

Lately, studies on transport mechanisms at pore scale with microfluidic devices have expanded due to their importance in many engineering applications (oil and gas production, groundwater pollution or wastewater treatment) and research topics (chemistry, biology, medicine). These devices, associated to novel imaging and visualization techniques, enable direct measurements and information on fluid behavior's complexity. Micromodels are 2D-microstructures made of transparent materials that allow the direct visualization of phenomena involved at the pore scale. In general, the access to the enclosed microstructure is provided by at least two holes that act as inlet and outlet ports. Etching patterns can be specifically designed according to the research objectives during the microfabrication process. To conduct experimental investigations of processes occurring in porous media, micromodels contain an artificial structure of interconnected pores that mimic the geometry of rocks. Pore-network patterns may be regular, partially regular or irregular. The internal structure of the micromodel may then be very diverse depending on the application.

Numerous studies were done to assess colloidal deposition and permeability damage using microfluidic devices (Auset and Keller, 2004; Bacchin et al., 2014; Delouche et al., 2020, 2022; Dersoir et al., 2017; Dincau et al., 2022; Duchêne et al., 2020; Hsu et al., 2017; Kim et al., 2022; Liu et al., 2019; Sauret et al., 2014, 2018). However, experiments are often conducted on simplified pore-network micromodel or microchannels with or without constrictions, that are not reproducing real porous media (Figure 1). This is mainly due to the complexity of the etching methods for the oldest works and the will to simplify models to understand the mechanisms. Investigations are made on flow behavior and deposition mechanisms around isolated obstacles or 2D arrays of pores and while these studies provide major insight into particle transport and clogging phenomenon, it does not include the complexity brought by the geometry of an irregular pore-network medium. A rock-like microstructure is marked by a heterogeneous geometry

that will significantly impact the tortuosity and connectivity of the porous medium, which in turn modifies greatly the velocity field and thus the properties of particle transport and deposition.

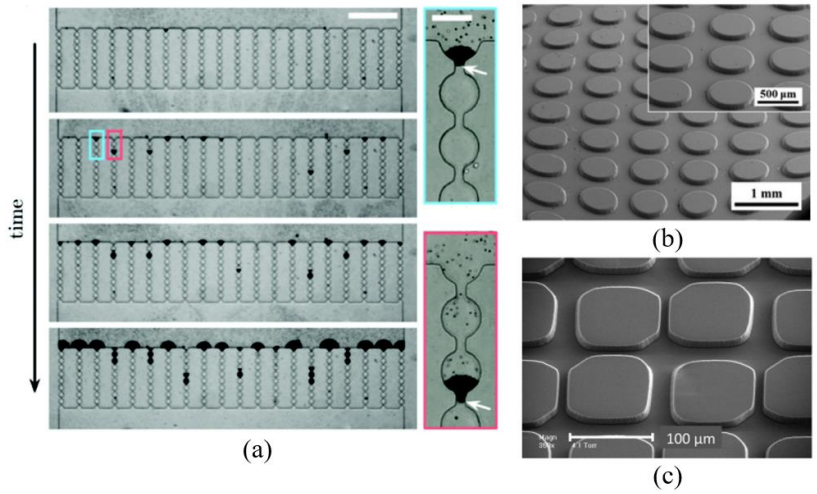

Figure 1 (a) Time lapse of a clogging experiment in a 20 parallel microchannels device. Flow goes from top to bottom. Particles appear in black and scale bar (in white) is 500 µm. The close-up views show clogs when a large contaminant blocks a microchannel at the entrance of further inside. The white arrows indicate the position of the large contaminants and scale bar is 50 µm (from Sauret et al., 2014); (b) Example of regular pattern (from Hsu et al., 2017); (c) Example of partially regular pattern (from Auset and Keller, 2004).

Hence, we focus our ongoing study on the injection of a diluted suspension of microspheres in a rock-like microstructure. A characterization system coupling direct visualization of the flow at the pore network scale with pressure measurement is used. In particular, the effects of geometry and particle concentration were studied. After introducing the fluid system and micromodel (dimensions and geometrical properties of the inner structure), we present the investigation protocol and the obtained results.

2. EXPERIMENTAL STUDY: MATERIALS AND METHODS

2.1 Fluid system

A stock suspension that contains fluorescent monodispersed polystyrene microspheres was purchased from Polysciences, Inc (Warrington, PA). The mean diameter of polystyrene microspheres in the suspension is 1 µm (coefficient of variation is 3%) and the density is 1.05 g/cm^3. As these particles are buoyant, sedimentation is avoided. The colloids are supplied in a 2.5% (w/v) aqueous solution (4.55 x 10^{10} particles/ml) and have carboxylate groups on their surfaces. Particles are thus negatively charged. The electrophoretic mobility of the polystyrene microspheres was measured using the Zetasizer Nano ZS from Malvern Instruments. At pH=5, the mean value was measured to -60mV, in agreement with previous studies using these microspheres (Makino et al., 2003). This specific surface coating associated with a negative electrophoretic mobility ensures that particles do not aggregate in solution before injection.

All particle suspensions are prepared with deionized (DI) water and colloid input concentration was adjusted by diluting the stock microsphere suspension to 100, 500 and 1000 mg/L respectively for the three experiments undertaken in this work.

2.2 Microfluidic Chip

A 45 mm × 15 mm microfluidic chip obtained from Micronit Microtechnologies (Enschede, Netherlands) was used in this study (Figure 2 (a)). The porous network is inspired by a 2D slice of a CT-scan image obtained from a real Bentheimer rock. The chip is made of borosilicate glass and as there is no additional surface coating made by the manufacturer, the micromodel is hydrophilic.

The inlet of the chip is a conical hole of which the bottom side is connected to a channel of 740 µm width. The channel is successively bifurcated into 540 µm width, followed by 440 µm and 340 µm width channels in the sequence; the length of these channels has been previously described (Pradhan et al., 2019). The subsequent eight channels are connected to a perpendicular channel of 500 µm width and 1 cm long which precedes the pore network of the microfluidic chip. The outlet side of the chip is connected to an exactly similar channel structure but in a reverse order. The advantage of this structure is that the pressure at the entrance of the porous medium is evenly distributed (in both directions of injection).

The inner porous network dimensions are 10 mm wide by 20 mm long (Figure 2 (b)) and the micromodel is 20 µm-deep.

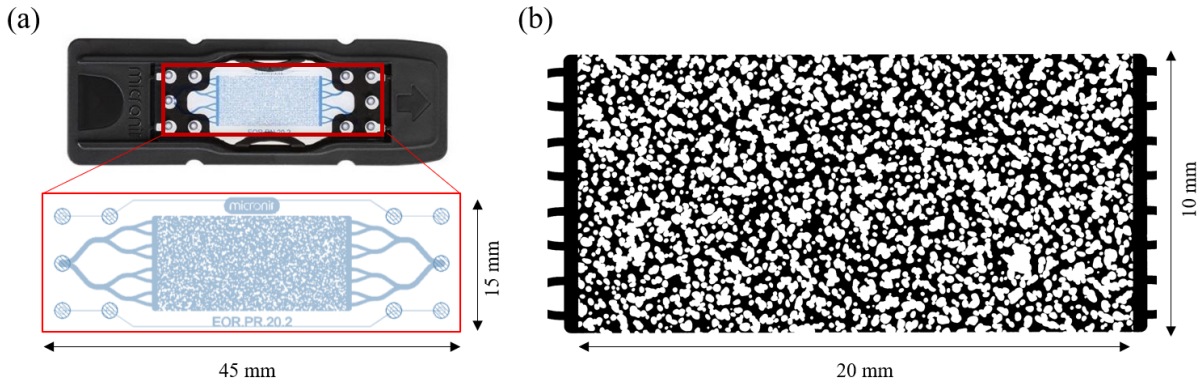

Figure 2 (a) Micronit chip and view of inlet and outlet ports; (b) Binarized model of the porous medium (grains appear in white while porous areas are black).

The physical and mechanical properties of rocks are dictated by several key parameters as their nature and internal structure. The sizes and distribution of pores play a determining role in the behavior of fluids flowing through the porous solid phases (Ehrlich and Kennedy, 1984). Throats serve as a connection between the pores and are therefore vital for the permeability.

2.2.1 Pore-network analysis

Thus, to understand its influence on macroscopic flow properties, we performed a quantitative analysis of the pore-throat network of the porous medium. Based on a binarized porous area of the micromodel, we used a modified version of the ImageJ watershed algorithm (Soille and Vincent, 1990; Yeates et al., 2019) to identify local distance minima between obstacles. These are the throats of the medium and the corresponding watersheds are assimilated to the pores. A sample of this decomposition is shown in Figure 3.

The total of obstacles assimilated to grains is 906 with an average grain radius equal to 146 µm and the overall porosity of the porous medium is 52.8%. The synthetic grain, pore and pore-throat size distributions are shown in Figure 3. The pore and pore-throat size distributions are slightly right skewed, as previously reported for carbonate and sandstone samples (Bloomfield et al., 2001; Liu et al., 2022; Steinwinder and Beckingham, 2019). As for other methods of investigation including micro-computed tomography (µ-CT), mercury intrusion porosimetry (MIP) or nuclear magnetic resonance, errors in pore-throat network distributions may result from limitations of image resolution (Shah et al., 2016; Zhang et al., 2018). However, errors induce by partial volume are avoided as micromodels are two-dimension objects.

Nevertheless, the pore-throat network distributions seem to mimic in a reasonable way the distributions observed for rock samples: they are extended over a wide range of values.

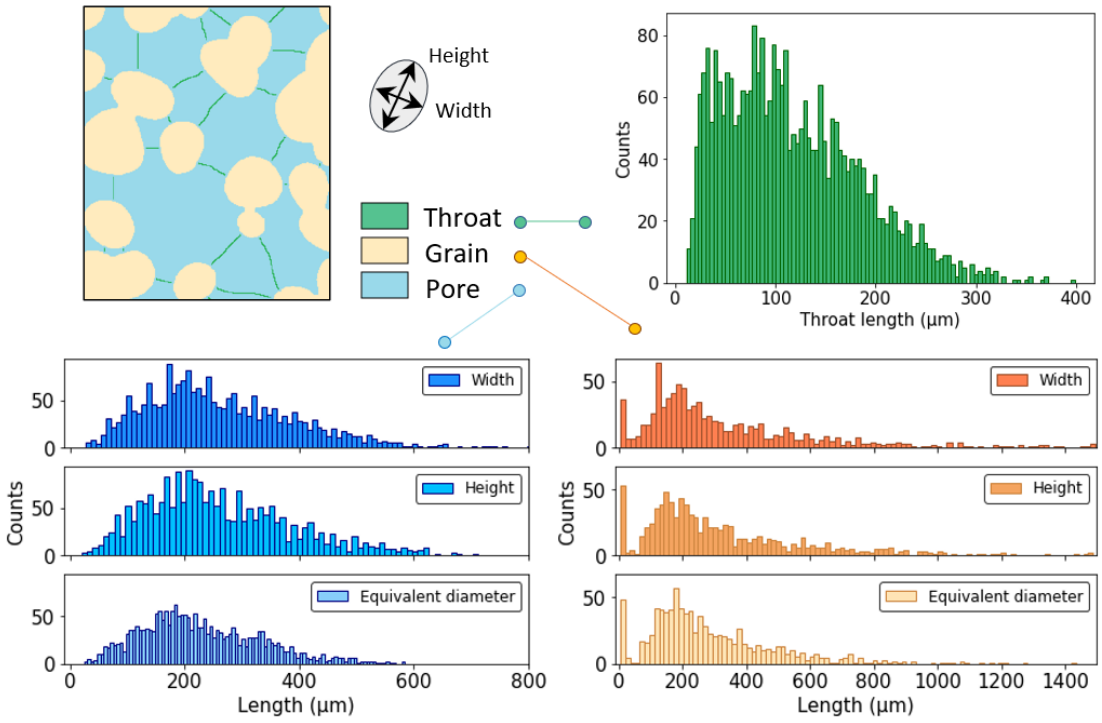

Figure 3 Sample of network decomposition on the left top corner and micromodel network characteristics. Mean values are 229 µm, 292 µm and 117 µm for the equivalent pore diameter, equivalent grain diameter and throat length respectively.

According to the International Union of Pure and Applied Chemistry (IUPAC) classification, pores of the porous medium we used in our work may be classified as macropores (size > 50 nm).

The corresponding mean of the pore and pore-throat size distributions are 229 and 117 µm respectively; the mean of throat radius is thus 58.5 µm, and 114.5µm is the average pore equivalent radius i.e., a ratio of approximately 2 between the two sizes.

The coordination number is a dimensionless number which refer to the number of throats connected to a single pore; the larger this number is, the better the connectivity. In addition, the increase of connectivity usually leads to increasing probability of forming highly conductive flow paths, enhancing the overall permeability of the porous medium (Dong and Blunt, 2009; Yuan, 1981). The distribution and the large average radius of pore suggest a good connectivity. For our porous medium, the number of pores amounted to 2144 while the number of throats is 2927, leading to an average coordination number of 1.4. This value lies in the range of coordination numbers obtained for carbonate and sandstone rock samples (Liu et al., 2022; Shah et al., 2016). 7% of pore bodies correspond to dead ends.

In addition, as the diameter of particles used in this work is 1 µm, the Throat to Colloid (TC) ratio has a similar distribution to the pore-throat distribution previously described.

2.2.2 Permeability

To complete our study on the geometric characteristics and petrophysical properties of the porous medium, the permeability of the micromodel was assessed using Darcy's law. For one-dimensional horizontal linear system, the rate of fluid flow is proportional to the hydraulic gradient and cross-sectional area, and inversely proportional to the viscosity of the fluid:

$$q = -\frac{kA}{\mu} \cdot \frac{\Delta P}{L} \quad (1)$$

where q, k, μ, A, L, Δp are volumetric fluid flow rate, absolute permeability, fluid viscosity, cross-sectional area, length and pressure gradient over the length L, respectively.

Thus, by collecting values of the pressure drop caused by fluid flow across the chip at different flow rates, the effective permeability can be obtained. In our study, DI water was used for the measurement and permeability was found to be 2 Darcy. However, this measurement takes into account the pressure drop along the entire chip i.e. the porous medium plus the inlet/outlet channels which have a much lower permeability than the porous medium. Simulations estimated the permeability of the porous medium alone at 10 Darcy.

2.3 Experimental set-up and procedure

Figure 4 presents the experimental set-up. Two pumps (Fluigent modular pressure-based flow controller and Strata DCP50 pump) ensure the injection of deionized water or of the colloidal suspension towards the microfluidic chip. The pressure drop across the micromodel is measured by ABB pressure sensors while a Zaiput back pressure regulator downstream is set at 2 bars. This choice allows us to minimize compressibility effects from the pressure gradient over the system and therefore enable a rapid saturation of the microfluidic chip. The optical device consists of a LED plate for backlighting the microfluidic chip and a Canon EOS-1D X camera whose CMOS sensor associated with a lens allows us to obtain high-resolution images (3µm/pixel) of the porous medium. In addition, an Avantes spectrophotometer with a specific application allowing on-line concentration measurements monitors the quantity of particles retained in the micromodel.

Although particles are buoyant, the colloidal suspension is agitated to avoid any sedimentation and the micromodel is flushed with an acetone solution before injection to prevent any difference of surface charge coating.

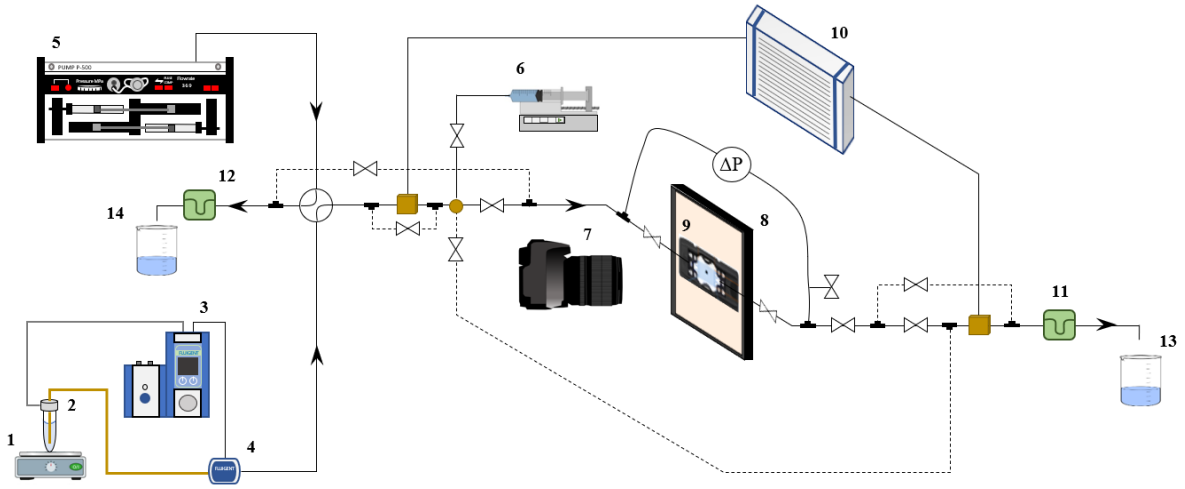

Figure 4 Schematic of the experimental set-up used for the injections. 1: stirrer; 2: colloidal suspension container; 3/4: Fluigent modular pressure-based flow controller; 5: Strata DCP50 pump; 6: syringe pump; 7: Canon camera; 8: LED plate; 9: microfluidic chip and holder; 10: Avantes spectrophotometer; 11/12: Zaiput backpressure regulators (single supply for both); 13/14: effluent recovery.

An experiment consists of continuously injecting a colloidal suspension in the microfluidic chip previously saturated with deionized water. A constant flow rate Q_0 = 25 µL.min^{-1} is imposed, meaning that the local velocity increases when the porosity decreases. The particle deposition in the porous medium is tracked thanks to image analysis and a recording of the pressure difference evolution during the experiment. Once the completion of the colloidal suspension injection is done, the inflow is switched back to deionized water to flush out the mobile colloids out of the porous medium and thus establish the mobility reduction due to particle clogging within the system.

2.4 Data analysis

We develop here the processing performed on the pressure and camera data.

2.4.1 Pressure data processing

Measurement of pressure difference over the course of the injection allows us to establish the reduction of permeability caused by transport and deposit of particles within the porous medium trough the mobility reduction coefficient R_m calculated as follows:

$$R_m = \frac{\Delta P_{injection} - \Delta P_0}{\Delta P_{DI\ water} - \Delta P_0} \quad (2)$$

With $\Delta P_{injection}$ the pressure difference (in mbar) measured during the injection of the colloidal suspension at Q_0=25 µL.min^{-1}, $\Delta P_{DI\ water}$ measured prior to the injection with DI water at the same flow rate and ΔP_0 the pressure difference measured across the micromodel (in mbar) when the injection rate is zero.

As the viscosity of the suspension is almost equal to that of the DI water and does not change during the injection, equation (1) becomes:

$$R_m = \frac{k_{injection}}{k_{DI\ water}} \quad (3)$$

Thus, the measurement of the mobility reduction coefficient can be assimilated to a measurement of the permeability reduction R_k. The evolution of R_m indicates the kinetics of particle deposition within the porous medium; if R_m increases, deposit increases.

2.4.2 Camera data processing

To access information at the pore scale and in relation to the optical resolution, we have chosen to focus the camera on an upstream zone of the porous medium (Figure 5 (a)). This zone corresponds to 20% of the porous medium area and the choice was validated by an analysis of the minimum representative area, particularly in terms of porosity.

Raw images consist of pixels whose values are set between 0 and 255 (black and white respectively). When particles are deposited in the medium, since the particles appear dark in the micromodel (Figure 5 (b)), the gray level decreases i.e., pixels values tend to 0. This changes the distribution of pixel values (Figure 5 (c)).

Based on the information above, image acquisition allows us to work with two quantities:

- Firstly, we determine the surface fraction represented by the deposit in the analysis window. In order to identify the deposit on the complete studied area, we used the segmentation method by thresholding, which consists in classifying the pixels according to whether their value is higher or lower than the threshold; this method produces a binary image regrouping these results (0 for the deposit, and 255 for pores and grains). Then, the ratio between black pixels and the total divided by the porosity can be established to obtain the surface fraction represented by the deposit within the pore space.
- Secondly, the normalized gray level was used to specifically track the deposition kinetics during the injection. To have a coherence between a deposition growth and pixel values distribution (when there is deposition, pixel values tend towards 0 so the gray level decreases), we used the inverse of the average gray level (Mean GV) calculated as follow:

$$Normalized\ Mean\ Gray\ Value\ = \frac{Mean\ GV_0}{Mean\ GV} \quad (4)$$

With GV_0 the average gray value of the analyzed zone when the injection starts i.e. no deposit is observed.

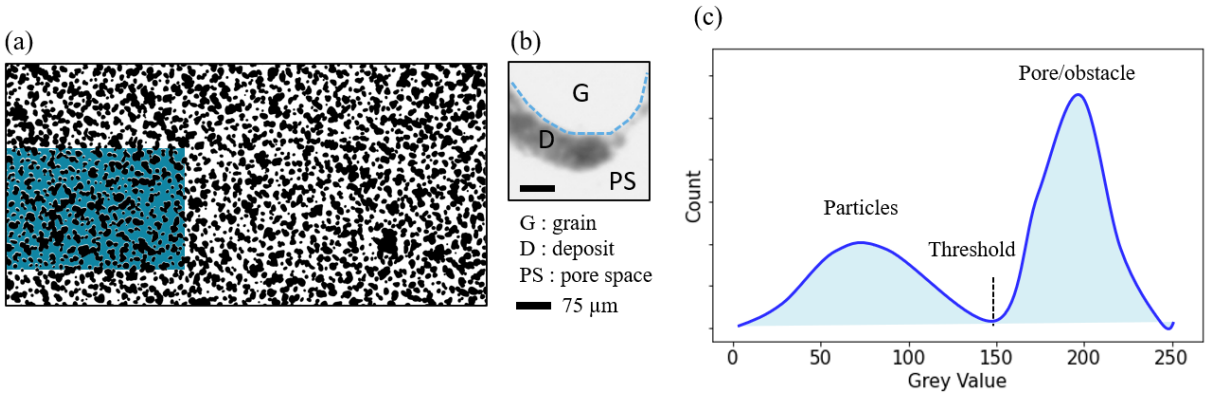

Figure 5 (a) Binarized model of the porous medium (20 mm × 10 mm). Grains appear in black, porous areas are in white and blue for the analysis window used in the following of this work; (b) Detail of a deposit observed during an injection of a colloidal suspension; (c) Schematic illustration of gray value distribution.

Uncertainties were estimated at 10% for image processing (thresholding) and 1% for physical data processing. Working with the mean gray value may then be more precise because it is not thresholded which is particularly relevant to evaluate the deposition kinetics.

Thus, at the end of an experiment, the recorded parameters are images allowing a quantitative analysis of deposit over time and the deposition kinetics as well as a measurement of the pressure difference from which we deduce the associated permeability reduction. Moreover, in order to compare the experiments conducted (at the same flow rate) with different particle concentrations, results are presented not in injected volume but in number of injected particles with the exception of a few results.

2.5 Modeling

We proceeded to the modeling of the porous medium in order to apprehend the effect of the pore-throat network and its complexity on flow velocities. The Navier-Stokes equation is solved for an incompressible single-phase flow formulation (Zhang et al., 2019, 2020). Solid phase of the porous medium is taken into account by a penalty method. The partial differential system is solved numerically by the in-house Fortran CFD code "Notus" (https://notus-cfd.org/), developed at the Institute of Mechanical Engineering (I2M-TREFLE). Notus is an open-source software based on the finite volume method. The variable fields are solved on a fixed staggered grid.

Result of this modeling is presented in Figure 6 which shows the complex distribution of velocities in the medium. Highest velocities (colors towards yellow and red) are associated to preferential paths while less connected areas of the network are associated to low velocities (blue areas).

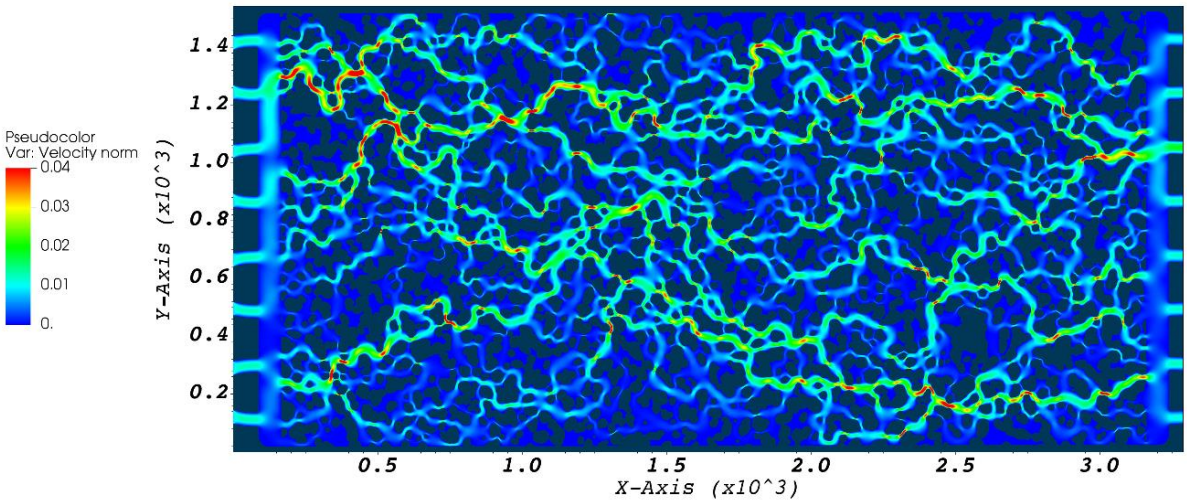

Figure 6 Fluid velocity distribution within the porous medium; grains are displayed in dark blue. Flow direction is from left to right.

In order to investigate the influence of hydrodynamics on the deposition process within the porous medium, 3 typologies strongly affected by the geometry of the porous medium were distinguished. The network and its complex geometry impact the local distribution of flow velocities: some zones are of low or high shear rates (highly supplied with particles) while others correspond to dead ends and are therefore not alimented by the flow (or very few).

These three typologies are defined as follows:

- Type I: low velocity flow area.
- Type II: intermediate velocity flow zone, in close proximity with a preferential flow area.
- Type III: high velocity area, may correspond to a preferential flow path, likely to be more subjected to hydrodynamics effects.

3. RESULTS & DISCUSSION

3.1 Injection of a 100 mg/L-concentrated suspension

A 100 mg/L particle suspension is injected at Q_0 = 25 µL min^{-1}. The results of this test are given on Figure 7 as the evolution of the mobility reduction coefficient (R_m – red curve) and surface fraction of the deposit (blue curve) vs the number of injected particles. R_m is a result of the measurement over the entire micromodel while the surface fraction of deposit is analyzed on a reduced window of the porous medium (see section 2.4)

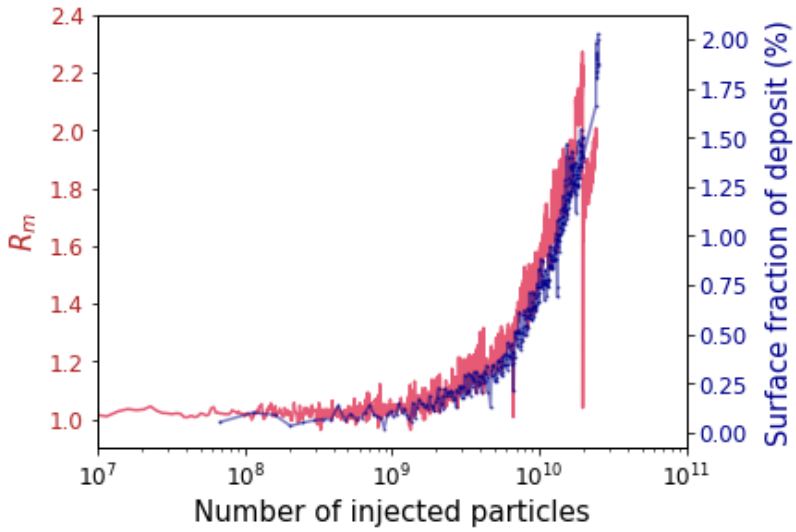

Figure 7 Dynamics of the surface fraction of deposit and mobility reduction (R_m) over the time of injection (number of injected particles).

At approximately 10^9 particles injected into the micromodel, the two observation parameters seem to indicate that the clogging dynamic has begun, the transient regime is over. At this concentration of 100 mg/L, there seems to be a good agreement between the R_m measurement and the visual observation of the deposit.

Looking more closely at the deposit within the window, while ~2.5x10^{10} particles were injected, the surface fraction of deposit only represents ~2% of the available pore space i.e. a minor portion. Figure 8 (a) and (b) show the close relationship between the more permeable, connected paths where the suspension will flow preferentially and the deposition zones. Low flow velocity areas are indeed associated with areas where no deposition could be identified, as shown by the area underlined in red. Deposit is essentially located in areas of intermediate flow velocities.

When the observation is made at the pore scale at the end of the suspension injection, the main deposition patterns correspond to total closures of the pore thresholds. The constriction is plugged, preventing any flow between the two now disconnected pores. This observation made on the 20%-representative window of the porous medium localized on the upstream part (Figure 8 (b)) can be specified at the pore scale (Figure 8 (c)) but also on the entire micromodel as shown on Figure 8 (d). This raw image of the micromodel taken after final water flushing allows to see many dark objects which correspond to clogged pore thresholds. At first sight, it seems that few thresholds are clogged but they correspond to key areas of the flow: depending on the geometry of the porous medium, each threshold will exert a different influence on the flow dynamics. In the case of the 100 mg/L injection and considering the final mobility reduction (R_m =2.2), it seems that the clogged pore thresholds are major elements for the flow.

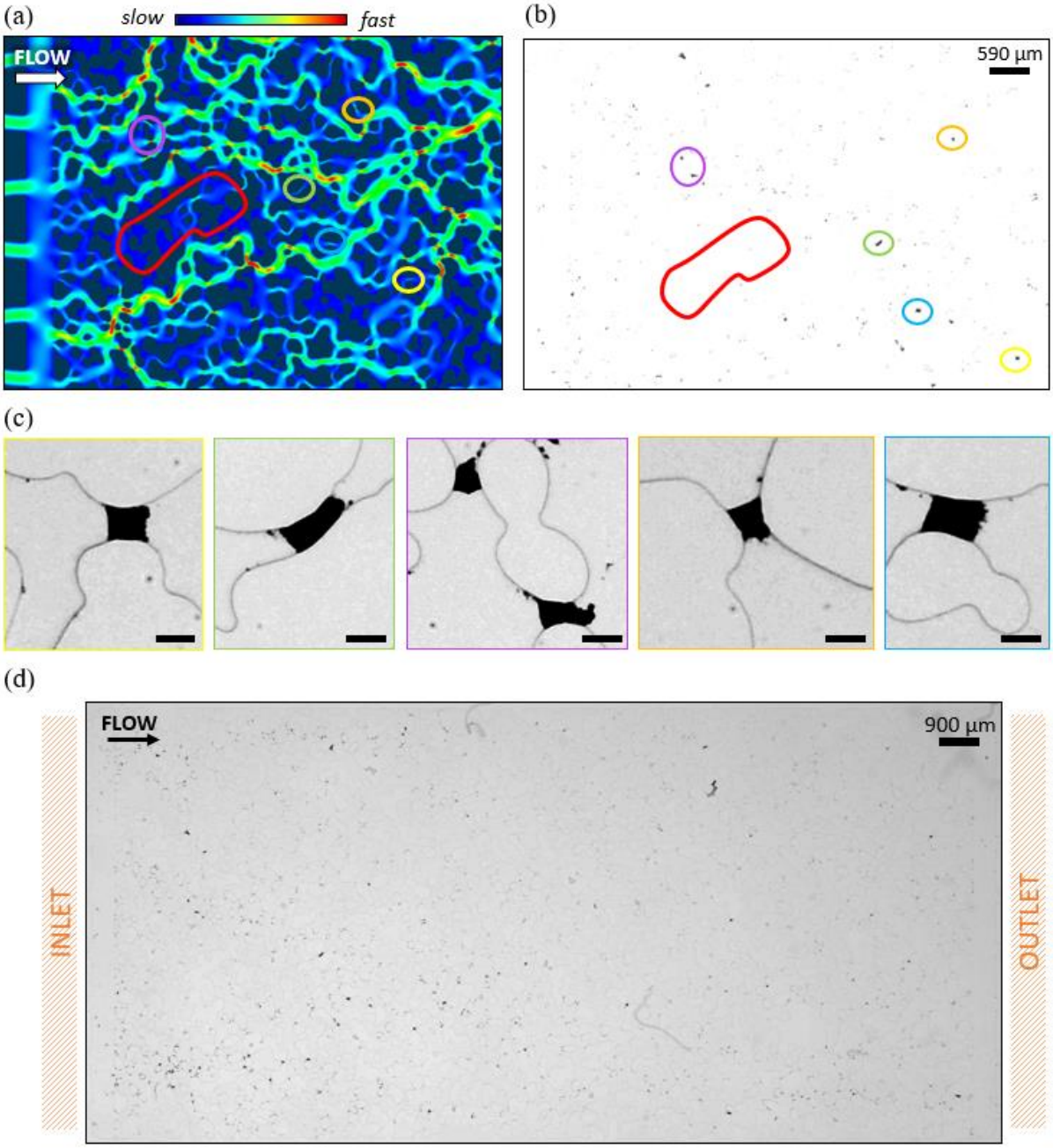

Figure 8 (a) Velocity field in analysis window (grains appear in black) before colloidal injection; (b) Window at the end of the suspension injection phase (deposit and clogs appear in black while fluid and solid phases are in white); (c) Zoom in (enhanced contrast for better visualization) of pore-throats clogs – colors correspond to those displayed in (a) and (b) figures, scale bar is 180 µm; (d) Non-processed image of micromodel after water flushing to assess permanent deposit. Deposit appears in strong black; some details on the upper and lower (slightly to the right) middle are artefacts associated to image acquisition.

Once the global dynamics are identified, it is interesting to look at the events that take place at the local scale. In order to investigate the mechanisms of deposition that lead to the closure of the pore throats, we have drawn profiles along the direction perpendicular to the flow. An example is shown in Figure 9.

The profiles, supported by the related images, indicate that deposition growth occurs on the collecting surfaces on either side of the pore threshold. Gradually, a layer is formed on both grains associated with the threshold that eventually leads to the construction of a multilayer deposit. This result is surprising considering that particles have carboxylate groups (negative charge) grafted to their surface which initiate a repulsion of the particles from each other and thus do not favor their deposition on the top of each other. The flow, in association with the geometry of the medium, seems to prevail over the repulsive nature of particle-particle interactions in the suspension. The gradual compression of streamlines facilitates the adhesive capture to pore walls and promotes multilayer deposition. Hydrodynamic forces due to fluid flow on the growing deposits are able to overcome the possible electrostatic repulsions between particles of the same charge and which are already deposited in the porous medium.

In light of the observed deposit figures, the formation of multi-layers by successive deposition of particles that aggregate seems to be the prevailing clogging mechanism. Eventually, the pore threshold is blocked.

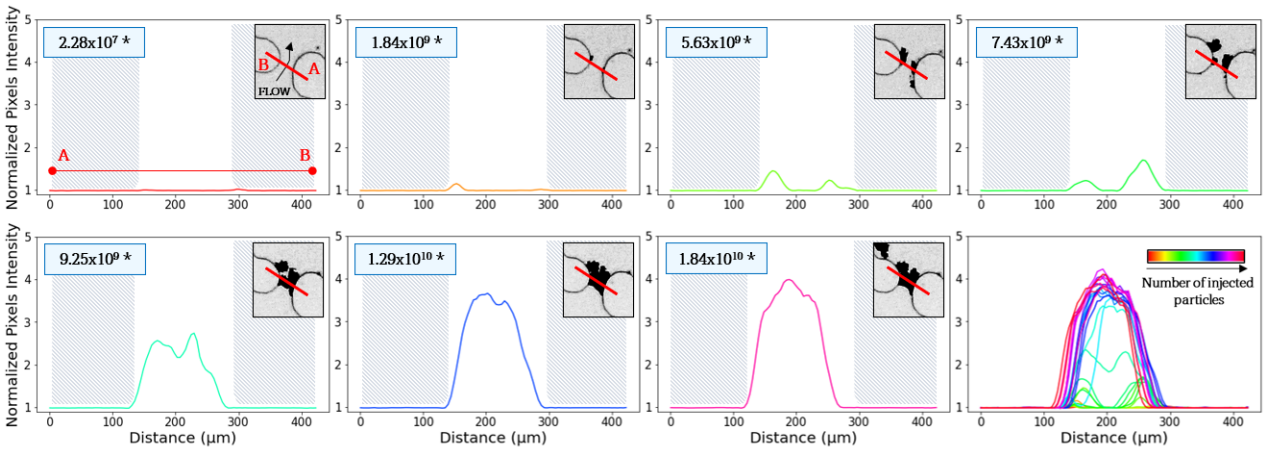

Figure 9 Growth profiles of a deposit at a pore threshold. For each profile, the number of particles injected is indicated and a corresponding image of the pore threshold (between A and B) is displayed. The last figure displays all profiles throughout the injection process. The black arrow indicates flow direction and the red mark indicates where the profile was realized. Gray areas correspond to solid phases (grain).

To assess the influence of the medium over the deposit, the evolution of the mean gray level is plotted over time for some areas belonging to one of the three typologies defined in section 2.5 (Figure 10 (a)). Window n°1 which corresponds to type I is located in the middle of a relatively low-velocities area (Figure 10 (b)). Y-scale may create an artefact on window n°1 and its curve evolution; a very flat slope exists and governs the dynamics of deposition by diffusion in this zone (Figure 10 (a)). Deposit does not occur on the surface of the collecting grains but corresponds to a progressive concentration of particles in this zone by diffusion as the flow proceeds (Figure 10 (c)). For type II, two observation windows numbered 2 and 3 were analyzed; these zones correspond to areas where flow velocities are relatively moderate but in proximity to high velocity flow zones (Figure 10 (b)). The observed deposit mechanism is a multilayer deposition which progressively leads to the reduction and then complete closure of the pore threshold (Figure 10 (c)).

The mean gray level for window 2 increases gradually and steadily as the flow progresses while the mean gray level for window 3 exhibits a sigmoidal shape with an inflection point when ~$1.4x10^{10}$ particles (~75 ml of suspension) have been injected. These evolutions indicate that the pores are in a stable flow environment that allows the perennial construction of the deposit. Finally, window 4 corresponds to a zone located on a preferential flow path where velocities are locally higher than for the previous zones (Figure 10 (b)). The mean gray level has an irregular trend with a more sawtooth-like evolution; particle deposition can occur but is unstable and as a result of locally higher flow velocities, no perennial construction is completed. The pore threshold is not clogged (window 4 Figure 10 (c)).

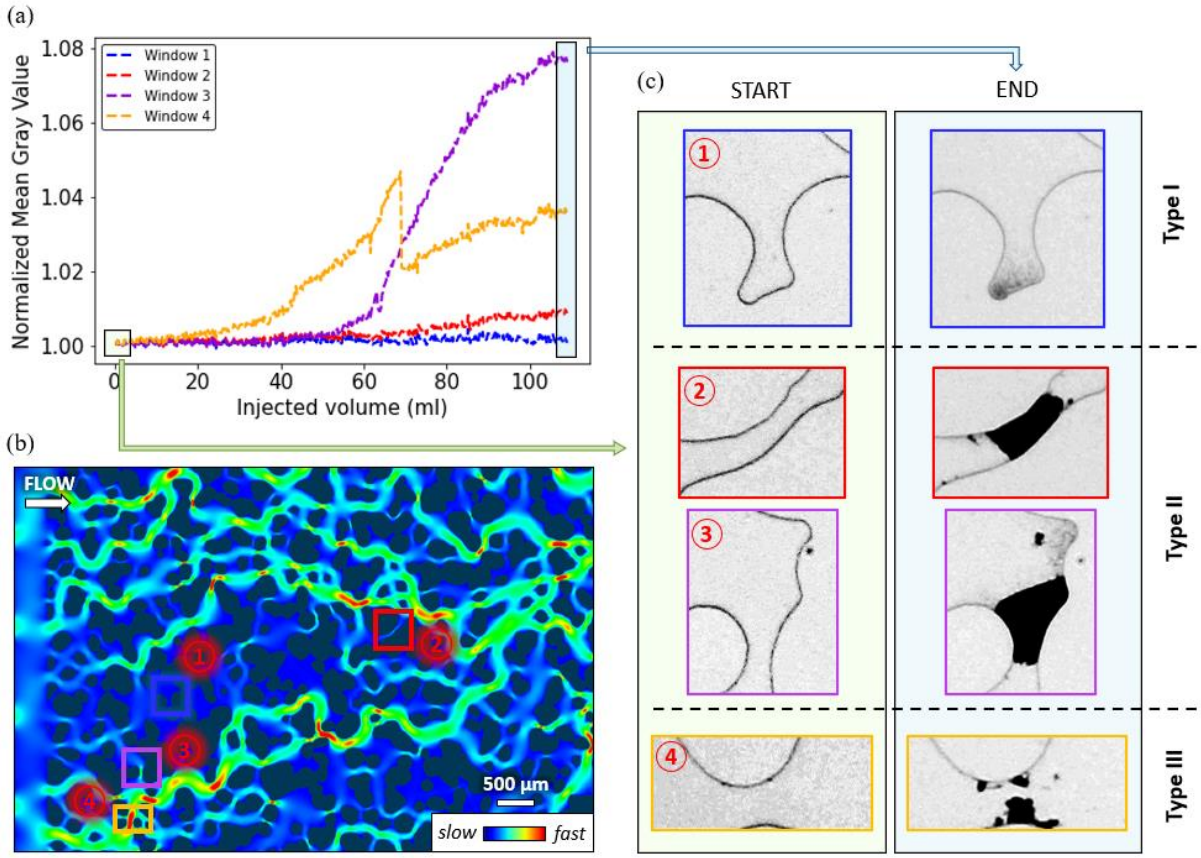

Figure 10 Injection of a 100 mg/L-concentrated suspension. (a) Evolution of the average grey level during injection, reflecting the local deposition dynamics for different analysis windows; (b) Fluid velocity distributions with analysis windows (grains appear in black) before colloidal injection; (c) Analysis windows at the beginning and end of the suspension injection, classified according to the typology of the flow area (enhanced contrast for better visualization).

As previously observed (Figure 7), the curve describing the surface fraction of the deposit within the observation window upstream of the porous medium correlates well with the mobility reduction coefficient (R_m). Nevertheless, what appeared to be a regular and progressive deposition at first sight may be decomposed into different deposition regimes linked to the porous medium geometry and to the location of the deposition zones in it. Indeed, Figure 10 allows us to see the different deposit occurring depending on the typology of the medium and the velocities associated to it. Pore-scale observations allow the decomposition of the global dynamics into multiple mechanisms (Figure 11): the global curve may be seen as a summary of several sub-curves with different kinetics due to the influence of the geometry of the porous medium on the local flow velocities.

For the four analyzed windows, deposit process seems to be initiated when the number of injected particles is higher than the one for the global kinetics (Figure 11). The graph shows the evolution of the surface fraction represented by the deposit for each of the analyzed windows as well as the global dynamics. At the end of the injection, the deposit can represent a significant part of the pore space (30% for window 3 and ~20% for window 4). However, the overall deposit on the 20%-surface window is not significant (black curve, 2% at the end of injection).

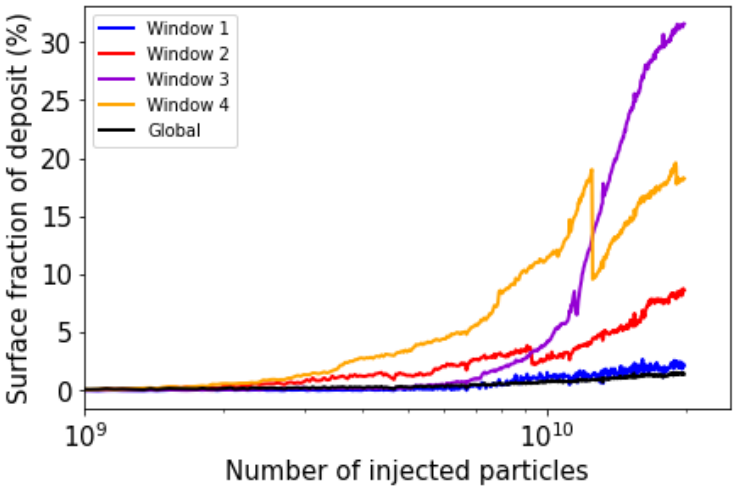

Figure 11 Comparison of the global dynamics of deposition and local dynamics (windows previously observed, representative of different typologies of flow areas). For each window, the surface fraction of deposit is scaled by the initial available pore space of the concerned window.

3.2 Injection of a 500 mg/L-concentrated suspension

A 500 mg/L particle suspension is injected at Q_0 = 25 µL min^{-1} as for the previous injection. The results are given on Figure 12.

The mobility reduction coefficient measured across the micromodel (R_m – red curve) and generated by the flow of the particle suspension within the micromodel appears once again similar to surface fraction of the deposit evolution (blue curve) in the chosen window. From ~$2x10^9$ particles injected in the micromodel, clogging of the porous medium is initiated: R_m curve seems to acquire an exponential dynamic. Image analysis indicates that deposits are large enough to be seen when ~$7x10^9$ particles were already injected; the discrepancy between the measured pressure difference and the visual data may be the result of first deposits occurring outside of the chosen window (which corresponds to 20% of porous medium).

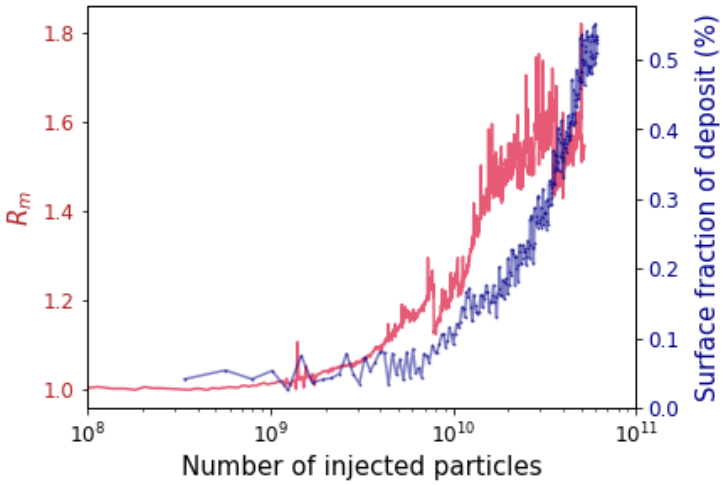

Figure 12 Dynamics of the surface fraction of deposit and mobility reduction (R_m) over the time of injection (number of injected particles).

In addition, although the number of particles injected is significant (~$6.1x10^{10}$ particles), the surface fraction of the deposit within the pore space in the analysis window represents only 0.52%, i.e. a very low percentage. However, mobility reduction reaches 1.8 which indicates that deposit, although relatively small, is located in critical zones for flow dynamics; because of their local pore network and connectivity, these zones have a major influence on permeability.

The main deposition patterns correspond to total closures of the pore thresholds (Figure 13(b)). The constriction is blocked and disconnect the two adjacent pores, preventing any particles flow between them. In addition, filamentous figures are locally observed; these forms of drapery are mainly located downstream of the grain in respect to flow direction. After the final water flushing carried out to evaluate permanent deposits, these filamentous figures are still present (Figure 13(c)), which differ from previously observed deposits i.e. clogged throats that were the only type of deposit and clogging figures. Visually, deposits appear to be larger than before and located upstream of the porous medium, in agreement with flow direction. However, mobility reduction measured at the end of the injection equals 1.8 and therefore indicates that these deposits, either because of their nature (filamentous, aggregate at the level

of a threshold) or by their location, are presumably less problematic for permeability reduction. Indeed, for this number of injected particles, R_m is higher for the previous injection while the suspension is 5 times less concentrated.

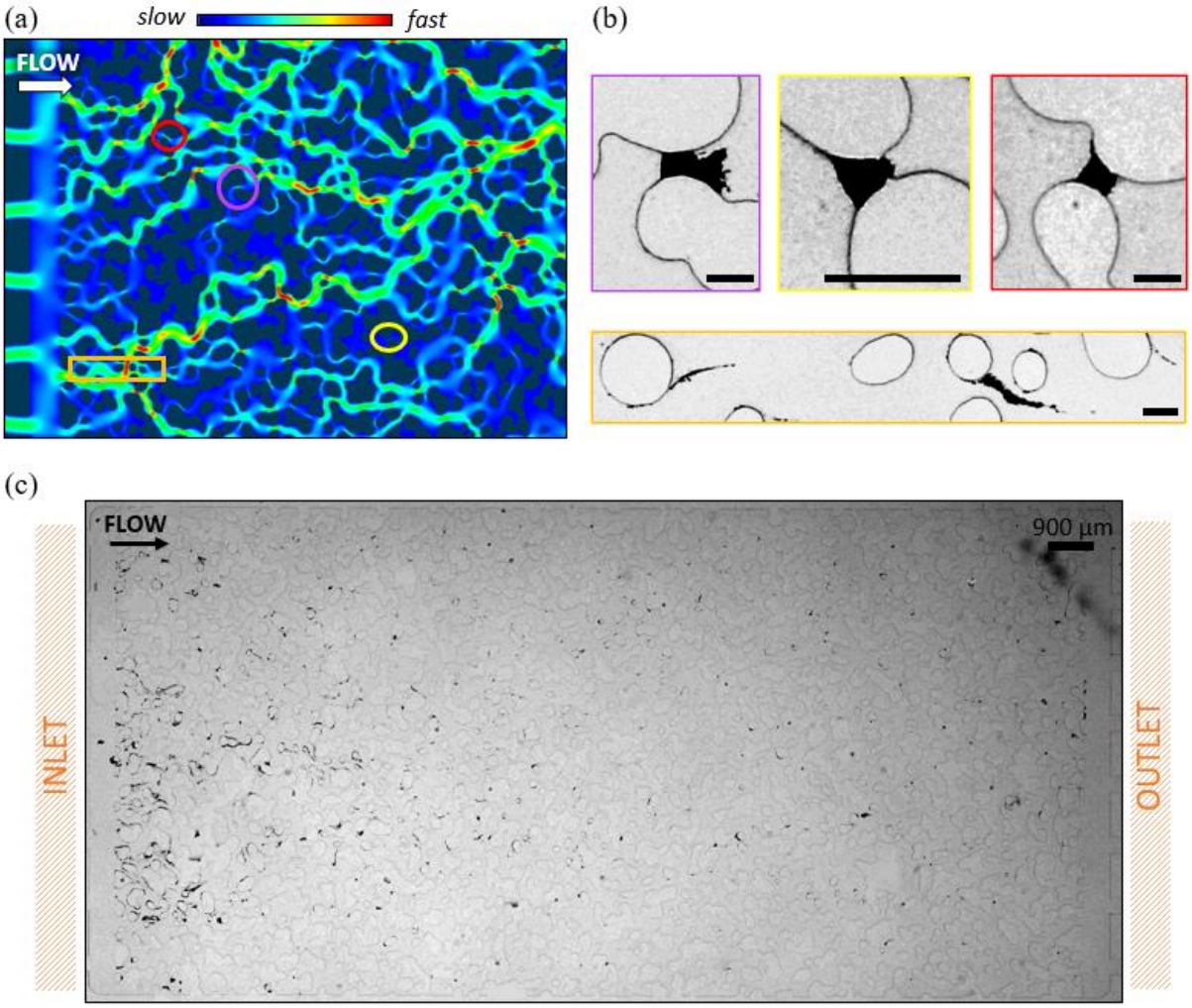

Figure 13 (a) Velocity field in analysis window (grains appear in black) before colloidal injection; (b) Zoom in (enhanced contrast for better visualization) of pore-throats clogs – colors correspond to those displayed in figure (a) and scale bar is 180 µm; (c) Non-processed image of micromodel after water flushing to assess permanent deposit. Deposit appears in strong black; some details are artefacts associated to image acquisition (black marks in the top right corner).

As previously done, deposit mechanisms may be investigated at pore thresholds by establishing deposit growth profiles, perpendicular to the flow direction. An example is shown in Figure 14. The profiles, supported by the related images, indicate that deposition growth occurs on the collecting surfaces on either side of the pore threshold (see plot 2 of Figure 14). Gradually, a layer is formed on both grains. Streamlines have a significant role in the deposit process and especially in the areas where particles will be trapped. Images show a downstream zone on the lower grain part that is gradually more filled with particles than its opposite i.e. the downstream zone of the upper grain. The local flow and associated streamlines create an exclusion zone where the gradual compression facilitates the adhesive capture to pore walls and particle-particle interactions. Eventually, the concerned threshold is clogged, the deposit is perennial, and the flow path is altered.

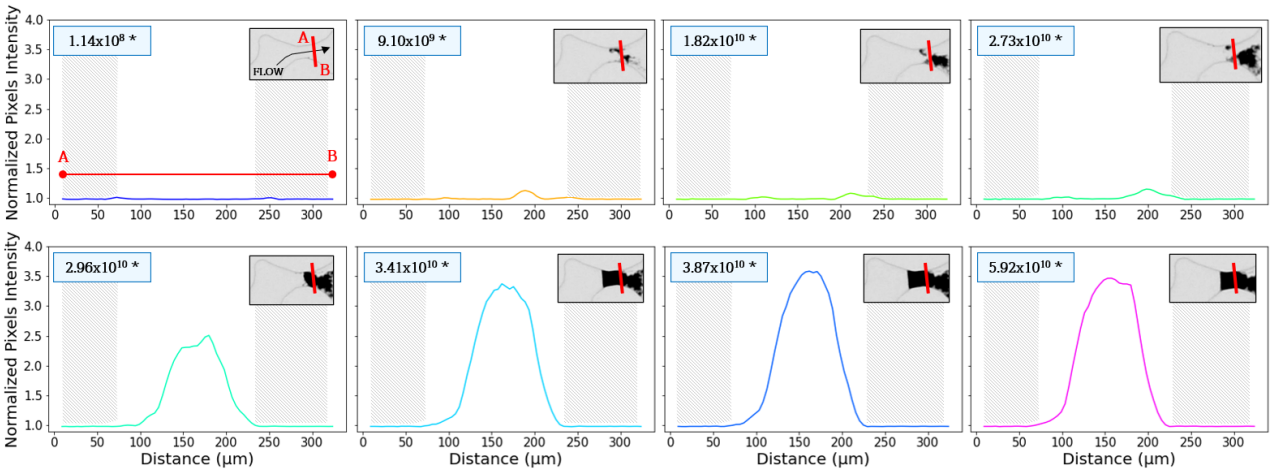

Figure 14 Growth profiles of a deposit at a pore threshold. For each profile, the number of particles injected is indicated and a corresponding image of the pore threshold (between A and B) is displayed. The black arrow indicates flow direction and the red mark indicates where the profile was realized. Gray areas correspond to solid phases (grain).

In order to investigate the influence of hydrodynamics stresses on the deposit processes within the porous medium when the initially injected suspension is more concentrated, the kinetics of the mean grey level were observed for four different areas corresponding to one of the three previously defined typologies.

Window 1 is focused on the same zone as the previous injection; corresponding to type I and located in the middle of a zone where the flow velocities are relatively low (Figure 15 (b)), the observed deposit corresponds to a progressive concentration of particles by diffusion as the flow progresses (Figure 15 (c)). A regular slope governs the dynamics of deposition by diffusion (Figure 15 (a)). For type II, two observation windows numbered 2 and 3 were chosen, with number 3 just downstream of window 2; these areas correspond to zones where flow velocities are relatively moderate but near preferential flow zones (Figure 15 (b)). Deposit process consists in a multilayer structure which progressively leads to the reduction and eventually the closure of the pore threshold (Figure 15 (c)).

Window 2 mean gray level increases very rapidly shortly after the beginning of the injection. From ~$9.1x10^9$ injected particles (~10 ml), the pore throat is clogged. The curve seems to have a sigmoid shape which may also be interpreted as a rising step shape. Similarly, window 3 curve evolution is marked by a gradual yet not significant beginning and then adopts a rising ramp or sigmoid shape with an inflection point when ~$2.7x10^{10}$ particles (~30 ml) have been injected. The two zones display the same clogging evolution and in view of their location (one after the other), experimental observations show that the first clogged pore constriction alters the flow patterns and may promote the clogging of the second pore further downstream. In addition, once these two pore thresholds clogged, the mean gray level display a stable evolution, as if a stationary regime had been reached. However, particles injection continues. As clogs do not grow in term of surface (no evolution of the gray level), it indicates that these areas are no longer positioned on a flow path; the deposit is perennial and these at-first key areas for deposit have become areas of non-circulating flow.

Finally, window 4 corresponds to a preferential flow path area where velocities are locally higher (Figure 15 (b)). The mean gray level has an irregular evolution; it increases steadily at the beginning and drops suddenly when ~$2.7x10^{10}$ particles (~30 ml) have been injected. Deposit may occur but is unstable and as a result of locally higher flow velocities, no perennial construction is completed. Pore thresholds of this analyzed area are not clogged (Figure 15 (c)) and particles aggregates seem to acquire a filamentary arrangement.

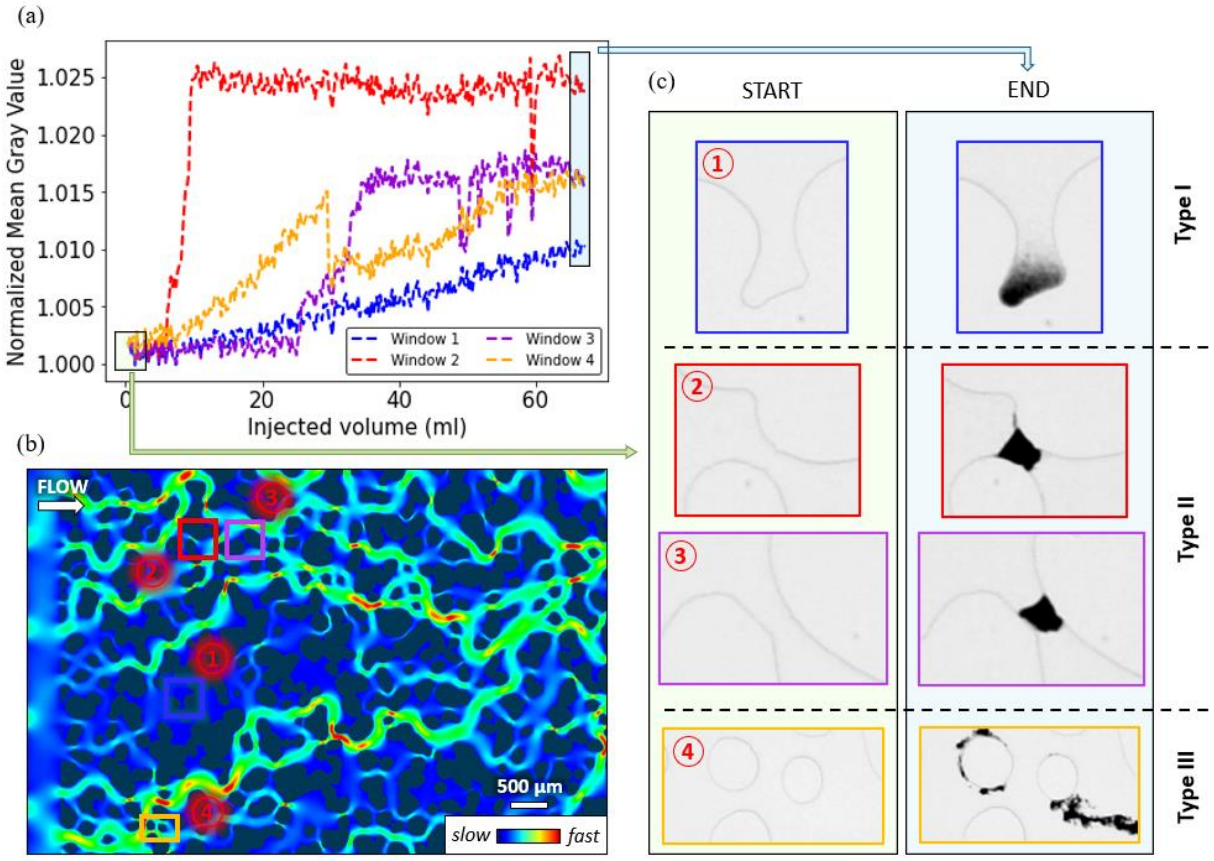

Figure 15 Injection of a 500 mg/L-concentrated suspension. (a) Evolution of the average grey level during injection, reflecting the local deposition dynamics for different analysis windows; (b) Fluid velocity distributions with analysis windows (grains appear in black) before colloidal injection; (c) Analysis windows at the beginning and end of the suspension injection, classified according to the typology of the flow area.

The surface fraction of the deposit within the general observation window (20% of the porous medium) correlates well with the mobility reduction coefficient R_m (Figure 12). If the global dynamics is progressive, it can be decomposed into different deposition regimes associated to the geometry of the medium and the local corresponding velocities. The observation at the pore scale allows to specify the global dynamics and to better perceive the complex mechanisms. Locally, behaviors of deposition mechanism are different according to the previously defined typologies as well as from the global kinetics (Figure 16). For type II, deposition occurs rapidly with clogging of window 2 starting at ~$5x10^9$ injected particles while the global dynamics starts at ~$7x10^9$ (Figure 12).

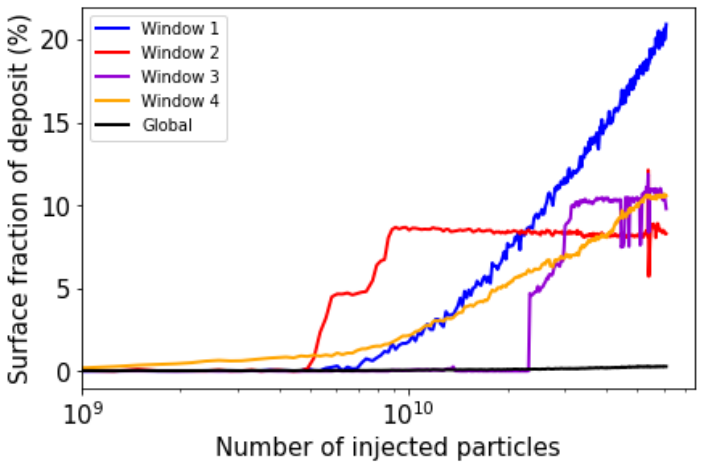

Figure 16 Comparison of the global dynamics of deposition and local dynamics (windows previously observed, representative of different typologies of flow areas). For each window, the surface fraction of deposit is scaled by the initial available pore space of the concerned window.

3.3 Injection of a 1000 mg/L-concentrated suspension

A 1000 mg/L particle suspension is injected at a similar flow rate i.e. Q_0 = 25 µL min^{-1}. The results are given on Figure 17 as the evolution of the mobility reduction coefficient and surface fraction of the deposit vs. the number of injected particles.

As for the other two previous injections, the mobility reduction coefficient measured across the micromodel (R_m - red curve) and generated by the flow of the particle suspension within the micromodel appears similar to the evolution of surface fraction of deposit (blue curve) in the chosen window. From ~$5x10^9$ particles injected in the micromodel, R_m curve seems to acquire an exponential dynamic: clogging of the porous medium is initiated. Image analysis indicates that deposits are large enough to be seen when ~ $2x10^9$ particles were already injected. When the completion of the suspension injection is done (~ 1.9 $x10^{11}$ injected particles), the reduction of permeability across the micromodel corresponds to R_k ~ 2.6.

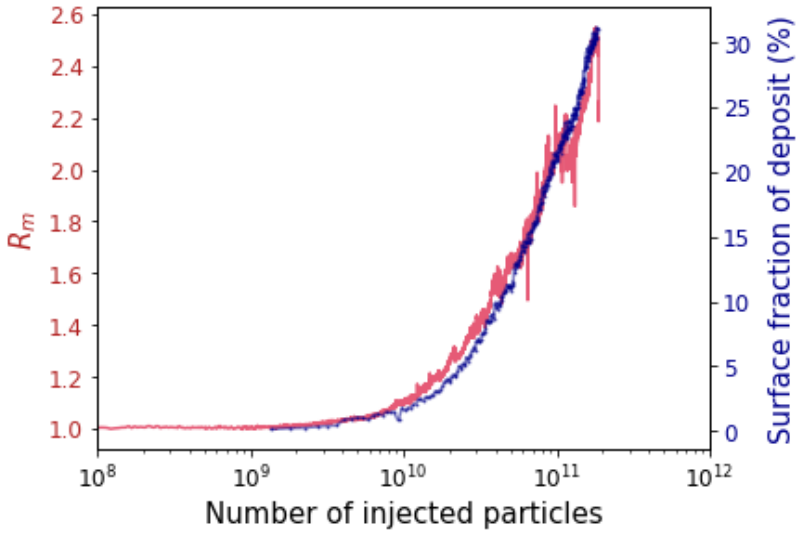

Figure 17 Dynamics of the surface fraction of deposit and mobility reduction (R_m) over the time of injection (number of injected particles).

In contrast to the previous injections (see section 3.1 and 3.2), the image processing indicates that the deposit represents 30% of the available pore space in the analyzed window, which is a much higher value than the precedent ones. Even with the same number of injected particles, deposit surface fraction values in the available pore space are higher for this 1000 mg/L injection than the two previous ones:

- At $2.5x10^{10}$ particles injected (end of 100 mg/L injection), deposit represents 5% vs. 2% (see section 3.1).
- At $6.1x10^{10}$ particles injected (end of 500 mg/L injection), deposit represents 12.5% vs. 0.5% (see section 3.2).

Hence, after injecting about $1.9x10^{11}$ particles, this 30% value obtained by image processing might seem particularly high; nevertheless, images of the upstream area and the micromodel well confirm this observation (Figure 18 (b) and (c)). The prevailing deposition patterns are filamentary patterns draping grains, and in particular surfaces directly subjected to the flow i.e., upstream faces. These cohesive objects of filament type represent several hundreds of microns in size and are deposited preferentially in pore-bodies. In the precedent injections, pore thresholds were the key geometries for deposition.

Comparison of the velocity field within the micromodel (Figure 18 (a)) and the deposit after injection seems to indicate a strong dependence between streamlines resulting from the flow and deposit location. Coupling between hydrodynamics and the medium geometry is thus particularly important and constitutes a key factor in the formation of deposits. In addition, as previously observed in the 100 mg/L and 500 mg/L injections, low flow velocity areas are associated with no deposition figures, as shown by the area underlined in red in Figure 18 (b).

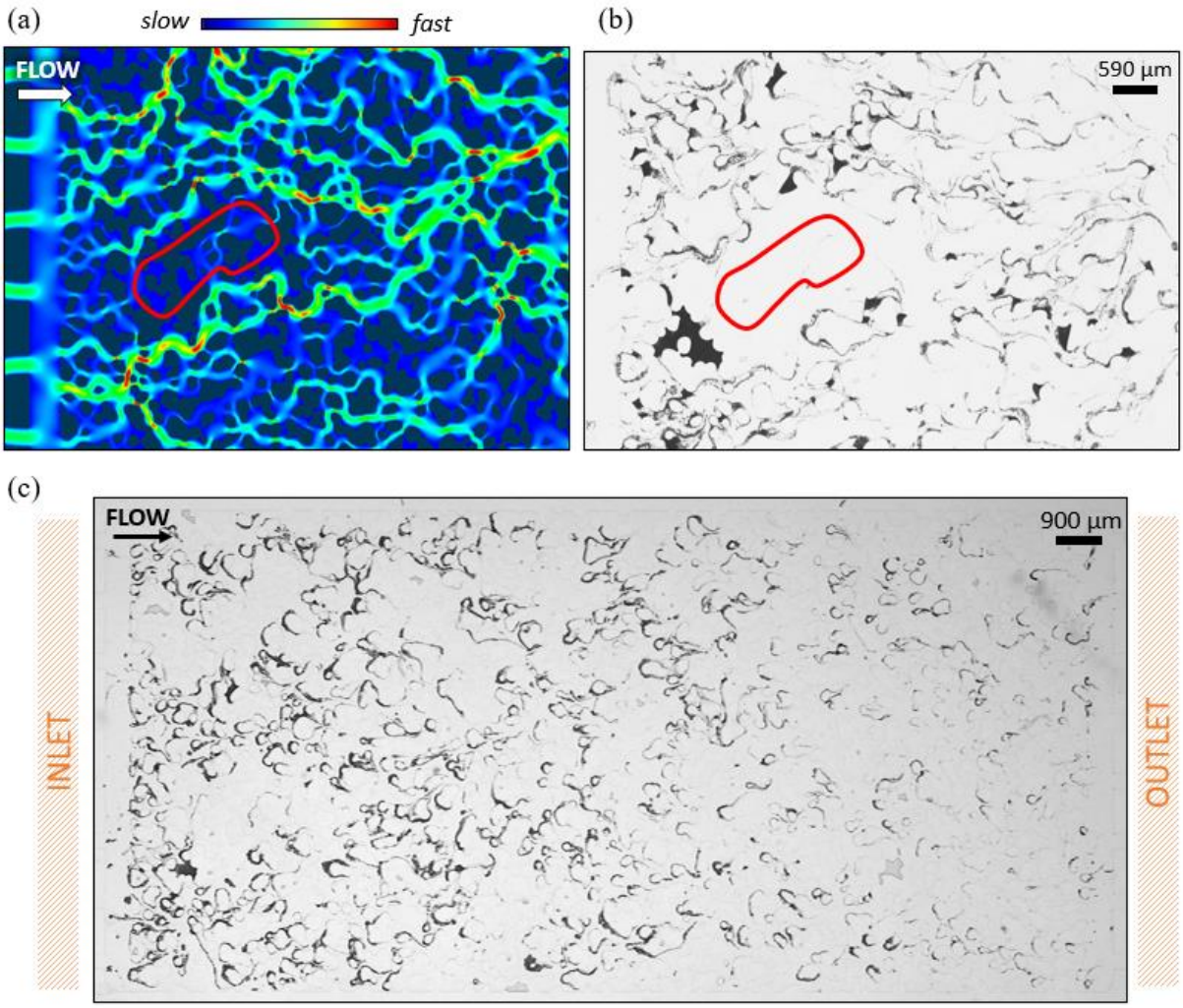

Figure 18 (a) Velocity field in analysis window (grains appear in black) before colloidal injection; (b) Window at the end of the suspension injection process (deposit and clogs appear in black while fluid and solid phases are in light grey); (c) Non-processed image of micromodel after water flushing to assess permanent deposit. Deposit appears in strong black; some details are artefacts associated to image acquisition.

Although the main deposition patterns appear different (filamentous) and occur mainly in pore bodies, pore thresholds are still subject to clogging. Hence, as previously done, deposit at pore thresholds is investigated by establishing deposit growth profiles, perpendicular to the flow direction. This allows us to determine if the deposit mechanisms in these thresholds remain identic. Profiles, supported by the related images, indicate that deposition growth occurs on the collecting surfaces on either side of the pore threshold and is influenced by flow direction and streamlines (Figure 19). Indeed, particles are captured at the pore/wall interface of a single grain at first (side of B grain). The multi-layer deposition takes place, and in a second step, the deposit construction starts on the other grain constituting the threshold. As indicated, the deposit is already present when 3.4×10^9 particles are injected which is consistent with the observation made on Figure 17 (surface fraction of deposit kinetics displays an increase when ~ 2×10^9 particles are injected). Considering the similar behavior displayed between R_m evolution and the surface fraction deposit, it seems that the clogging of the pore threshold analyzed here is one of the elements accountings for the permeability reduction.

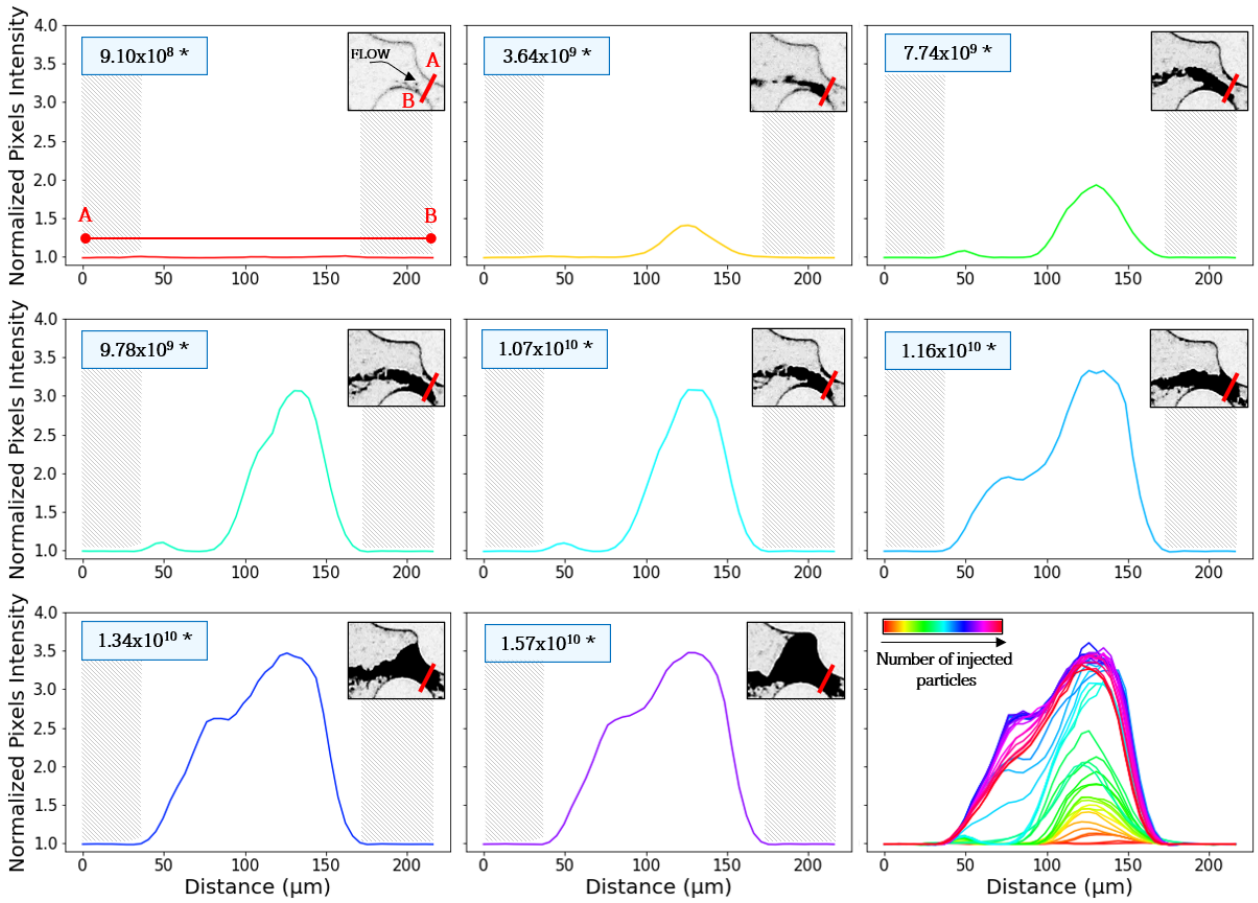

Figure 19 Growth profiles of a deposit at a pore threshold. For each profile, the number of particles injected is indicated and a corresponding image of the pore threshold (between A and B) is displayed. The last figure displays all profiles throughout the injection process. The black arrow indicates flow direction and the red mark indicates where the profile was realized. Gray areas correspond to solid phases (grain).

We also investigated the influence of hydrodynamics on the deposit processes as the input concentration of microspheres increase in four different areas classified as one of the three typologies defined in section 3.1.

Window 1 corresponding to type I is focused on a low flow velocities area. The observed deposit corresponds to a progressive concentration of particles as the injection is still going on (Figure 20 (c)). The chosen y scale does not permit to clearly visualize the gray level evolution of window 1 during the injection but we can notice a regular slope that governs the dynamics of deposition until the mean gray level reaches a plateau when ~18.75 ml of the suspension ($3.4x10^{10}$ particles) is injected in the micromodel. The normalized average gray value is then constant, around 1.004.

One window is considered for type II (n°2) and correspond to an area located in an intermediate flow velocity zone, in proximity to preferential flow areas (Figure 20 (b)). The area is characterized by the formation of a multilayer structure on both side of the pore threshold which eventually leads to the reduction and closure of this section. Particles accumulate upstream of the clog and progressively fill the pore body (Figure 20 (c)). The deposit process acquires a similar dynamic to the area considered for type I (diffusion process) with a regular slope. As the two curves display similar kinetics, the rate of construction is likely to be equal although the type of deposit is different.

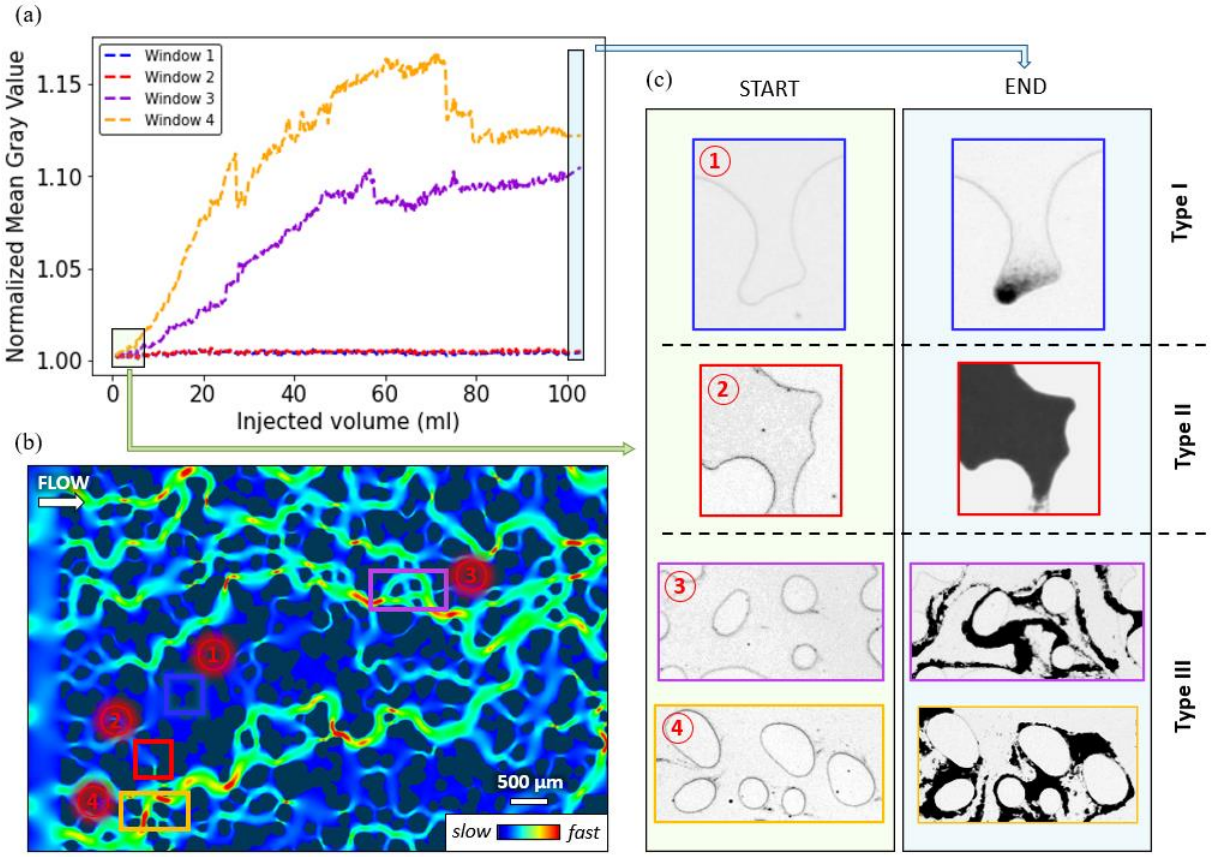

Figure 20 Injection of a 1000 mg/L-concentrated suspension. (a) Evolution of the average grey level during injection, reflecting the local deposition dynamics for different analysis windows; (b) Fluid velocity distributions with analysis windows (grains appear in black) before colloidal injection; (c) Analysis windows at the beginning and end of the suspension injection, classified according to the typology of the flow area.

As for type III, two areas were considered (windows n°3 and 4) They are located on preferential flow paths with local high velocities (Figure 20 (b)) in which filamentous objects draping grains are observed. For this injection, it is the prevailing deposition type. As it was previously observed for window 4 of the 500 mg/L injection, the mean gray level has an irregular evolution for both observed windows. Window 3 is not located in the most upstream slice of the porous medium but further in. The area is therefore particularly subject to events taking place further upstream. Between 10 and 30 ml injected, the curve evolution is marked by steps with several small leaps where the mean gray level increases quickly as a response of an event occurring in the area (Figure 20 (a)). Indeed, filamentous objects built upstream may have been removed and transported to the analyzed area, thus clogging the pore space. Window 4 is centered on an upstream zone of the porous medium (Figure 20 (b)). The mean gray level is irregular, it increases and drops on several occasions (~25 ml and ~75 ml for example) (Figure 20 (a)). The deposit occurs but is unstable and no perennial construction is completed. Aggregates are built at pore surfaces and due to stripping forces, are then removed and transported further downstream in the porous medium. Sudden drops in the curve are the result of these stripping effects and local high flow velocities that destabilize the filamentous objects. Figure 21 shows images of the analyzed windows during these particular jump points. Despite the uncertainty resulting from the data processing, the corresponding images make it possible to clearly visualize stripping and deposit mechanisms at work in the porous medium. At the end of the injection, experimental observations show that, in these preferential flow paths, deposit takes the form of filaments (Figure 20 (c)).

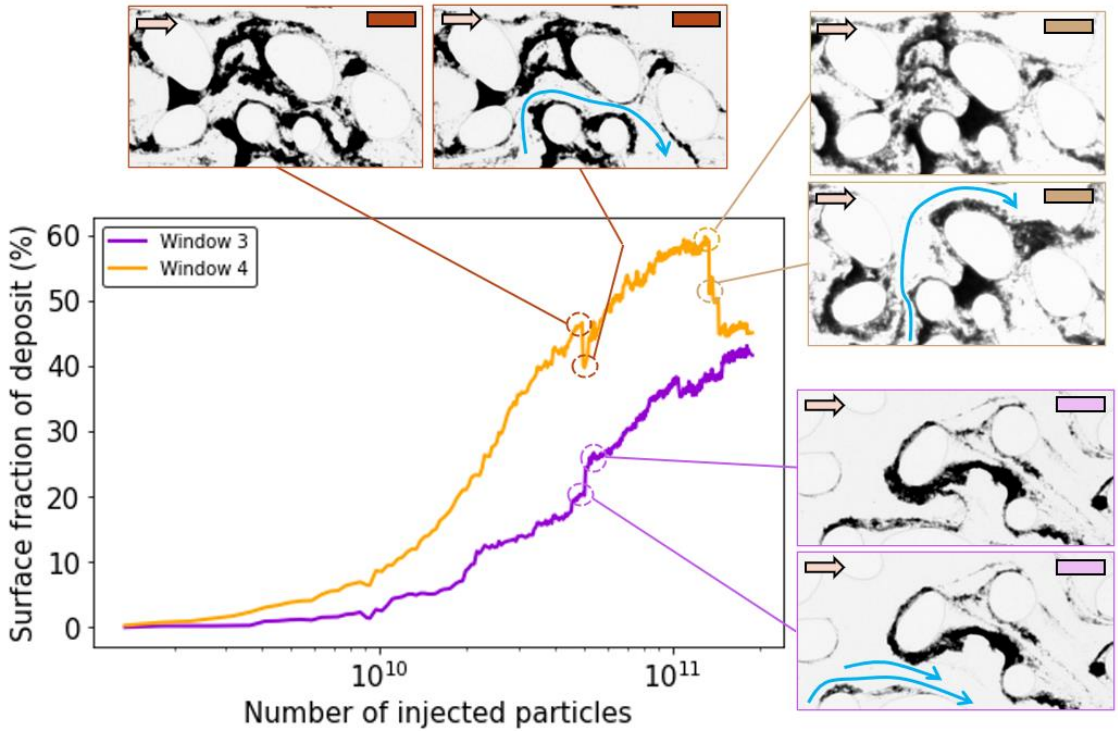

Figure 21 Illustrations of stripping and displacement effects of the aggregates. Deposit and clogs appear in black while fluid and solid phases are in light grey. Scale bar is 375 µm for all analyzed windows. The light red arrow indicates the flow direction. Blue arrows indicate either the new path created by stripping of an aggregate or the areas where these may have been deposited.

Local observations allow a better understanding of mechanisms governing the global dynamics of clogging within the porous medium. For this injection of a 1000 mg/L-concentrated suspension, Figure 22 displays the evolution of the deposit surface fraction of the 20%-micromodel window and the evolution for the four different areas previously analyzed. Once again, local behaviors appear different of the global one. Deposition occurs more rapidly in type III areas (window 3 and 4 – purple and yellow curves respectively) while deposit in type I and II areas (low or intermediate velocity areas) is concurrent to the global kinetics. The pore space in window 2 (red curve) is filled with particles; the flow continued through this section and therefore particles agglomerate upstream of the clog that take on the role of an internal filter cake.

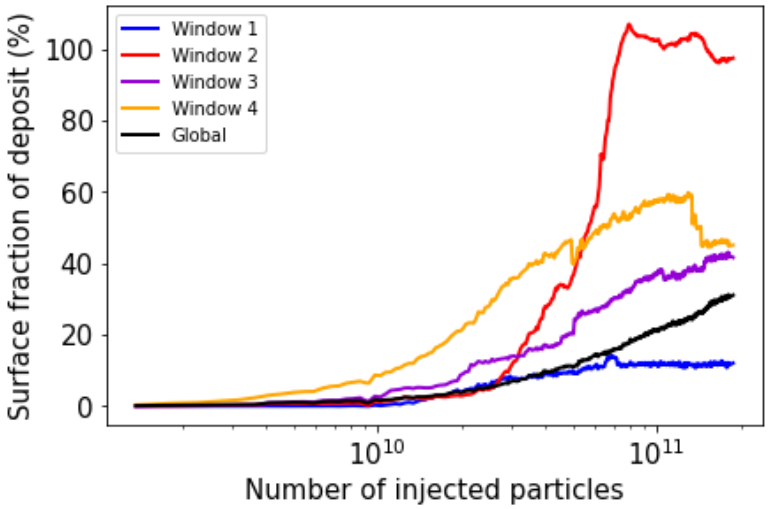

Figure 22 Comparison of the global dynamics of deposition and local dynamics (windows previously observed, representative of different typologies of flow areas). For each window, the surface fraction of deposit is scaled by the initial available pore space of the concerned window.

3.4 Comparison of three injections

The comparison of the three injections highlights the impact of concentration increase on the permeability reduction kinetics (Figure 23); the latter is indeed delayed, i.e. for the same number of injected particles, the least concentrated suspension (100 mg/L) causes the most damage in the porous medium. Although the damage kinetics acquires an exponential form for the three injections, the threshold number of injected particles before clogging begins appears to increase with the concentrations: 10^9, $2x10^9$ and $5x10^9$ particles for the 100, 500 and 1000 mg/L suspension concentrations respectively. This result may appear surprising. For the three injections, the flow rate and the porous medium are identical so that the number of pore thresholds likely to be clogged is the same. However, at high concentration, the local viscous forces are probably different. Thus, the increase of the apparent viscosity may favor local stripping mechanisms: the multilayer deposit constructed at these thresholds is stripped and rebuilt many times before it is permanently stable. This may explain the delay of the global kinetics between the injection of a low-concentrated suspension and a high-concentrated suspension.

The comparison between the evolution of the mobility reduction coefficient and the evolution of the surface fraction of deposit in the available pore space allowed us to observe that clogging due to a gradual growth of the deposit at the threshold is a greater threat to the reduction of permeability than a previously stripped aggregate that may clog a pore throat. The latter is more likely to be permeable and then act as an internal filter cake. However, caution must be taken, as the formation of an external filter cake may then occur (Tale et al., 2021) and represent an equally important danger for the porous medium permeability.

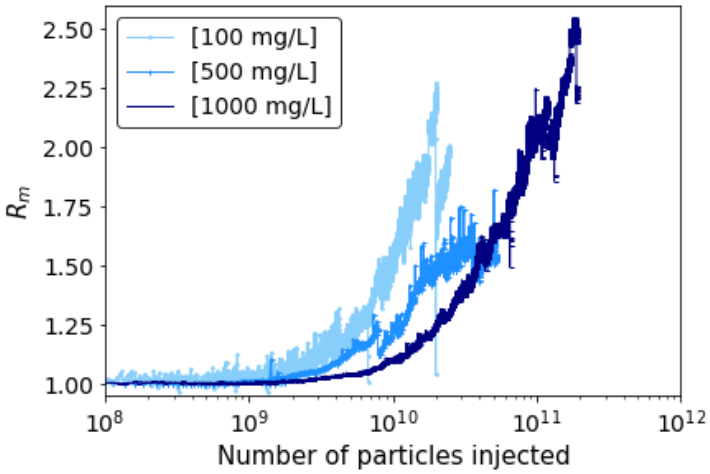

Figure 23 Comparison of permeability reduction dynamics for the three tested concentration of particles in suspension (light, medium and dark blue for 100, 500 and 1000 mg/L respectively).

In addition, this ongoing study has allowed us to evaluate the impact of the porous medium geometry on fluid flow behavior. The heterogeneity of the medium seems to favor aggregation, with filamentous deposition patterns particularly visible at high concentration.

In light of these results and observations, further work seems essential to understand the influence of external forces that allow the aggregation of negatively charged particles that should not aggregate. In particular, the local study of streamlines during injection and deposit formation could enable us to understand whether the hydrodynamic forces are high enough to overcome the electrostatic repulsions.

4. CONCLUSION

Clogging experiments were undertaken using a micromodel whose inner geometry correspond to a rock-like porous medium. The pore-throat network displays a complex geometry that is associated to a wide velocity field distribution as observed through modeling. The direct observation allows the comprehension of the different steps leading to the formation of the deposit in a tortuous yet connected medium, that eventually leads to a permeability reduction.

With a low concentration of particles in the suspension, permeability reduction is due to the progressive construction of a multilayer deposit at pore thresholds which leads to the closure of the latter. The deviation of streamlines may then induce deposition at a location that was not a preferential flow and deposition area. The increase in concentration induces a delay in the permeability reduction kinetics and new figures of deposit. Filamentous forms are observed within the pore bodies and seem to be more strongly subjected to hydrodynamic forces. A progressive plugging of the available pore space occurs and results in the formation of a dense superficial deposit that acts as an internal cake: the suspension continues to flow through, and particles accumulate upstream of the clog. For all, experimental results suggest that capture and deposit of polystyrene microspheres at pore-walls are velocity field-dependent and hydrodynamic stresses are locally high enough to overcome the electrostatic repulsions between particles of the same charge. This behavior is more important when concentration increases.

As indicated by other studies (Bacchin et al., 2014; Bizmark et al., 2020), experiments show that hydrodynamics effects are significant and have to be taken into account, especially for simulations performed for a quantitative description of the clogging dynamic. Their dual role may promote deposit or stripping behavior. In addition, the results reveal how the porous medium geometry control the distribution of colloids.

5. REFERENCES

Auset, M., & Keller, A. A.: Pore-scale processes that control dispersion of colloids in saturated porous media: COLLOID DISPERSION AT PORE SCALE. *Water Resources Research*, **40**(3), (2004).

Bacchin, P., Derekx, Q., Veyret, D., Glucina, K., & Moulin, P.: Clogging of microporous channels networks: role of connectivity and tortuosity. *Microfluidics and Nanofluidics*, **17**(1), (2014), 85–96.

Bizmark, N., Schneider, J., Priestley, R. D., & Datta, S. S.: Multiscale dynamics of colloidal deposition and erosion in porous media. *Science Advances*, **6**(46), (2020), eabc2530.28

Bloomfield, J., Gooddy, D., Bright, M., & Williams, P.: Pore-throat size distributions in Permo-Triassic sandstones from the United Kingdom and some implications for contaminant hydrogeology. *Hydrogeology Journal*, **9**(3), (2001), 219–230.

Delouche, N., Dersoir, B., Schofield, A. B., & Tabuteau, H.: Flow decline during pore clogging by colloidal particles. *Physical Review Fluids*, **7**(3), (2022).

Delouche, N., Schofield, A. B., & Tabuteau, H.: Dynamics of progressive pore clogging by colloidal aggregates. *Soft Matter*, **16**(43), (2020), 9899–9907.

Dersoir, B., Schofield, A. B., & Tabuteau, H.: Clogging transition induced by self filtration in a slit pore. *Soft Matter*, **13**(10), (2017), 2054–2066.

Dincau, B., Tang, C., Dressaire, E., & Sauret, A.: Clog mitigation in a microfluidic array via pulsatile flows. *Soft Matter*, **18**(9), (2022), 1767–1778.

Dong, H., & Blunt, M. J.: Pore-network extraction from micro-computerized-tomography images. *Physical Review. E, Statistical, Nonlinear, and Soft Matter Physics*, **80**(3 Pt 2), (2009), 036307.

Duchêne, C., Filipe, V., Huille, S., & Lindner, A.: Clogging of microfluidic constrictions by monoclonal antibody aggregates: role of aggregate shape and deformability. *Soft Matter*, **16**(4), (2020), 921–928.

Ehrlich, R. & Kennedy, S. K.: Petrographic image analysis, I. analysis of reservoir pore complexes. *Journal of Sedimentary Research*, **54**, (1984).

Hsu, S.-Y., Zhang, Z.-Y., & Tsao, C.-W.: Thermoplastic micromodel investigation of two-phase flows in a fractured porous medium. *Micromachines*, **8**(2), (2017), 38.

Jahanbakhsh, A., Wlodarczyk, K. L., Hand, D. P., Maier, R. R. J., & Maroto-Valer, M. M.: Review of microfluidic devices and imaging techniques for fluid flow study in porous geomaterials. *Sensors* (Basel, Switzerland), **20**(14), (2020), 4030.

Kim, D. Y., Jung, S. Y., Lee, Y. J., & Ahn, K. H.: Effect of colloidal interactions and hydrodynamic stress on particle deposition in a single micropore. *Langmuir: The ACS Journal of Surfaces and Colloids*, **38**(19), (2022), 6013–6022.

Liu, H., Ma, C., & Zhu, C.: X-ray micro-CT based characterization of pore-throat network for marine carbonates from South China Sea. *Applied Sciences* (Basel, Switzerland), **12**(5), (2022), 2611.

Liu, Q., Zhao, B., & Santamarina, J. C.: Particle migration and clogging in porous media: A convergent flow microfluidics study. *Journal of Geophysical Research: Solid Earth*, **124**(9), (2019), 9495–9504.

Makino, K., Yamamoto, N., Higuchi, K., Harada, N., Ohshima, H. & Terada, H.: Phagocytic uptake of polystyrene microspheres by alveolar macrophages: effects of the size and surface properties of the microspheres. *Colloids and Surfaces B: Biointerfaces*, **27**(1), (2003), 33–39.

Pradhan, S., Shaik, I., Lagraauw, R., & Bikkina, P.: A semi-experimental procedure for the estimation of permeability of microfluidic pore network. *MethodsX*, **6**, (2019), 704–713.

Sauret, A., Barney, E. C., Perro, A., Villermaux, E., Stone, H. A., & Dressaire, E.: Clogging by sieving in microchannels: Application to the detection of contaminants in colloidal suspensions. *Applied Physics Letters*, **105**(7), (2014), 074101.

Sauret, A., Somszor, K., Villermaux, E., & Dressaire, E.: Growth of clogs in parallel microchannels. *Physical Review Fluids*, **3**(10), (2018).

Shah, S. M., Gray, F., Crawshaw, J. P., & Boek, E. S.: Micro-computed tomography pore-scale study of flow in porous media: Effect of voxel resolution. *Advances in Water Resources*, **95**, (2016), 276–287.

Soille, P., & Vincent, L. M.: Determining watersheds in digital pictures via flooding simulations. *Proceedings of Visual Communications and Image Processing '90: Fifth in a Series Conference*, SPIE, Lausanne, Switzerland (1990).

Steinwinder, J., & Beckingham, L. E.: Role of pore and pore-throat distributions in controlling permeability in heterogeneous mineral dissolution and precipitation scenarios. *Water Resources Research*, **55**(7), (2019), 5502–5517.

Tale, F., Kalantariasl, A., & Malayeri, M. R.: Estimating transition time from deep filtration of particles to external cake during produced water re-injection and disposal. *Particulate Science and Technology*, **39**(3), (2021), 312–321.

Yeates, C., Youssef, S., & Lorenceau, E.: New insights of foam flow dynamics in a high-complexity 2D micromodel. *Colloids and Surfaces A: Physicochemical and Engineering Aspects*, **575**, (2019), 184–198.

Yuan, H.: The influence of pore coordination on petrophysical parameters. *Proceedings of SPE Annual Technical Conference and Exhibition*. SPE 10074, San Antonio, Texas, USA (1981).

Zhang, F., Erriguible, A. and Marre, S.: Investigating laminar mixing in high pressure microfluidic systems. *Chem. Eng. Sci.*, **205**, (2019), 25–35.

Zhang, Z., Kruschwitz, S., Weller, A., & Halisch, M.: Enhanced pore space analysis by use of μ-CT, MIP, NMR, and SIP. *Solid Earth*, **9**(6), (2018), 1225–1238.

Zhang, F., Marre, S. and Erriguible, A.: Mixing intensification under turbulent conditions in a high pressure microreactor, *Chem. Eng. J.*, **382,** (2020), 122859.